A Supplement

A.1 Tables

Table S1: Reactions used in the computational microglia model.

Rxn No.	Rxn	Cell	Reference
1	$Ca_i^{2+} \to CaM \to CN$	Cardiac	Heineke and Molkentin (2006); Bazzazi et al. (2015)
2	$P2X4 \to Ca_i^{2+}$	Microglia	Toulme and Khakh (2012); Garcia-Guzman et al. (1997)
3	$P2X7 \to Ca_i^{2+}$	Microglia	Khadra et al. (2012b); Chessell et al. (1997)
4	$Ca_i^{2+} \to pp38$	Microglia	Trang et al. (2009)
5	$Ca_i^{2+} \to SERCA$	Microglia	Shannon et al. (2004)
6	$Ca_{ER}^{2+} \to Calreticulin$	Astrocytes	Shannon et al. (2004)
7	$Ca_e^{2+} \to Ca_i^{2+}$		Fitted
8	$Ca_{ER}^{2+} \to Ca_i^{2+}$		Fitted
9	$pp38 \to TNF\alpha$	Microglia	Hide et al. (2000)
10	$NFAT\ cycle$	Myocyte	Cooling et al. (2009)
11	$NFAT \to TNF\alpha$	Microglia	Nagamoto-Combs and Combs (2010)
12	$CN \to NFAT$	Microglia	Zawadzka et al. (2012); Cooling et al. (2009)
13	$NCX \to Ca_e^{2+}$	Microglia	Shannon et al. (2004)

Table S2: Experimental data and ATP stimuli used for model validation.

Case	Cell Type	P2X Type	ATP Stimulation	Reference
Fig. 2A	C8-B4 microglia	P2X4	30 secs	Toulme and Khakh (2012)
Fig. 2B	Mouse microglia	P2X7	1.5 secs	Chessell et al. (1997)
Fig. 3	Rat microglia	P2X4/7	8 mins (varies)	Hide et al. (2000)
Fig. 4	Mouse microglia	P2X7 & P2Z/Y	Varies	Ferrari et al. (1999*b*)
Fig. 5	Rat microglia	P2X4	Varies	Trang et al. (2009)
Fig. 6A	Rat microglia	P2X4/7	3 hrs	Hide et al. (2000)
Fig. 6B	Rat microglia	P2X4/7	Varies	Hide et al. (2000)
Fig. S3	Rat microglia	N/A	Varies	Boscia et al. (2009)

Table S3: Markov State Parameters for P2X4 and P2X7 Receptors used to generate Fig. 3A. The rest of parameters for P2X7 is given in Sect. A.3.1.

Parameter	Value	Unit	Reference & Note
$H1_{P2X4}$	2.00×10^{-5}	ms^{-1}	Fitted
$H2_{P2X4}$	2.60×10^{-4}	ms^{-1}	Fitted
$H6_{P2X4}$	1.30×10^{-4}	ms^{-1}	Fitted
$k1_{P2X4}$	1.00×10^{-3}	ms^{-1}	Fitted
$k2_{P2X4}$	2.61×10^{2}	$\mathrm{M}^{-1}\,\mathrm{ms}^{-1}$	Fitted
$k3_{P2X4}$	1.00×10^{-2}	ms^{-1}	Fitted
$k4_{P2X4}$	1.65×10^{2}	$\mathrm{M}^{-1}\,\mathrm{ms}^{-1}$	Fitted
$k5_{P2X4}$	2.50×10^{-4}	ms^{-1}	Fitted
$k6_{P2X4}$	8.00×10^{3}	$\mathrm{M}^{-1}\,\mathrm{ms}^{-1}$	Fitted
$E12_{P2X4}$	0	V	Zemkova et al. (2015)
$G12_{P2X4}$	2.05×10^{-13}	$\mathrm{C}\,\mathrm{ms}^{-1}\,\mathrm{V}^{-1}$	Fitted
$H1_{P2X7}$	5.00×10^{-6}	ms^{-1}	Fitted
$H2_{P2X7}$	2.00×10^{-4}	ms^{-1}	Fitted
$k1_{P2X7}$	3.94×10^{-5}	ms^{-1}	Fitted
$k2_{P2X7}$	8.00×10^{-1}	$\mathrm{M}^{-1}\,\mathrm{ms}^{-1}$	Fitted
$k3_{P2X7}$	2.00×10^{-4}	ms^{-1}	Fitted
$k5_{P2X7}$	4.00×10^{-5}	ms^{-1}	Fitted
$E12_{P2X7}$	0	V	Khadra et al. (2012)
$G12_{P2X7}$	1.00×10^{-11}	$\mathrm{C}\,\mathrm{ms}^{-1}\,\mathrm{V}^{-1}$	Fitted
$V_{P2X4/P2X7,rev.pot.}$	-5.00×10^{-2}	V	Boscia et al. (2009)
$f_{I_{Ca},P2X4}$	8.24×10^{-2}		Garcia-Guzman et al. (1997)
$f_{I_{Ca},P2X4}$	1.00×10^{-1}		Adapted from Garcia-Guzman et al. (1997)
$f_{conv.P2X4}$	11		Factor to estimate the intracellular Ca^{2+} concentration based on the inward current via activated P2X4 channels
ρ_{P2X4}	1		Entity proportional to surface density of P2X4
ρ_{P2X7}	1		Entity proportional to surface density of P2X7

Table S4: Reversal potentials and channel densities used in Markov State models of P2X4 and P2X7 receptors: fitted to individual P2X channels Toulme and Khakh (2012); Chessell et al. (1997) in Fig. 2

Case	Parameter	Value	Unit	Reference & Note
Fig. 2A	$V_{P2X4,rev.pot}$	-6.00×10^{-2}	V	Toulme and Khakh (2012)
	ρ_{P2X4}	30		Toulme and Khakh (2012)
	r_{MG}	2.68	μm	Radius of Microglia at resting state Kongsui et al. (2014)
Fig. 2B	$V_{P2X7,rev.pot}$	-6.00×10^{-2}	V	Chessell et al. (1997)

Table S5: Parameters used in Markov State Models of P2X7 receptor: fitted to inward current measured from P2X7 channels by Chessel Chessell et al. (1997) in Fig. 2B

Parameter	Value	Unit	Reference & Note
$H1_{P2X7}$	5.00×10^{-6}	ms^{-1}	Fitted
$H2_{P2X7}$	2.00×10^{-4}	ms^{-1}	Fitted
$H7_{P2X7}$	6.20×10^{-5}	ms^{-1}	Fitted
$k1_{P2X7}$	3.94×10^{-5}	ms^{-1}	Fitted
$k2_{P2X7}$	1.00	$M^{-1}\,ms^{-1}$	Fitted
$k3_{P2X7}$	2.00×10^{-3}	ms^{-1}	Fitted
$k4_{P2X7}$	1.18	$M^{-1}\,ms^{-1}$	Fitted
$k5_{P2X7}$	8.00×10^{-4}	ms^{-1}	Fitted
$k6_{P2X7}$	15.0	$M^{-1}\,ms^{-1}$	Fitted

Table S6: Parameters for Calculations associated with Buffers Parameter

Parameter	Value	Unit	Reference & Note
$k_{ab,CaMCN}$	5.00×10^{-2}	$\mu M^{-2}\,ms^{-1}$	Fitted from Bazzazi et al. (2015)
$k_{ba,CaMCN}$	5.00×10^{-2}	ms^{-1}	Fitted from Bazzazi et al. (2015)
$k_{bc,CaMCN}$	8.00	$\mu M^{-2}\,ms^{-1}$	Fitted from Bazzazi et al. (2015)
$k_{cb,CaMCN}$	0.80	ms^{-1}	Fitted from Bazzazi et al. (2015)
$k_{off,A,CaMCN}$	0.16	ms^{-1}	Fitted from Bazzazi et al. (2015)
$k_{off,B,CaMCN}$	8.00×10^{-3}	ms^{-1}	Fitted from Bazzazi et al. (2015)
$k_{on,A,CaMCN}$	80.0	$\mu M^{-1}\,ms^{-1}$	Fitted from Bazzazi et al. (2015)
$k_{on,B,CaMCN}$	1.60×10^{-2}	$\mu M^{-2}\,ms^{-1}$	Fitted from Bazzazi et al. (2015)
CNt	2.00	μM	Total amount of free calcineurin Bazzazi et al.
$CaMt$	3.00	μM	Total amount of free calmodulin Bazzazi et al.
$B_{max,Fura}$	25.0	μM	Adapted from Shannon et al. (2004): Fura-2 related
$K_{on,Fura}$	1.50×10^{-1}	$\mu M^{-2}\,ms^{-1}$	Paredes et al. (2009)
$K_{off,Fura}$	2.30×10^{-2}	ms^{-1}	Paredes et al. (2009)
$B_{max,Calr,ER}$	140	μM	Shannon et al. (2004): Calreticulin related
$k_{on,Calr,ER}$	0.10	$\mu M^{-2}\,ms^{-1}$	Shannon et al. (2004)
$k_{off,Calr,ER}$	65.0	ms^{-1}	Shannon et al. (2004)
$B_{max,B,extra}$	10	μM	Fitted: Extra Buffer other than named
$k_{on,B,extra}$	1.0	ms^{-1}	Fitted
$k_{off,,B,extra}$	1.0	$\mu M^{-1}\,ms^{-1}$	Fitted

Table S7: Parameters for NCX and SERCA Calculations

Parameter	Value	Unit	Reference & Note
Ca_e	2.00×10^3	μM	Shannon et al. (2004)
$C_{mem,MG}$	1.20×10^{-11}	F	Est. from Nguyen et al. (2017); Toulme and Khakh (2012)
$H_{Na,NCX}$	3.60		Shannon et al. (2004)
$Kd_{Act,NCX}$	4.00×10^{-2}	μM	Fitted
$K_{max,Ca_i,NCX}$	3.59	μM	Shannon et al. (2004)
$K_{max,Ca_e,NCX}$	1.30×10^3	μM	Shannon et al. (2004)
$K_{max,Na_i,NCX}$	1.23×10^4	μM	Shannon et al. (2004)
$K_{max,Na_e,NCX}$	8.75×10^3	μM	Shannon et al. (2004)
Na_e	1.45×10^5	μM	Shannon et al. (2004)
Na_i	8.00×10^3	μM	Shannon et al. (2004)
$Q_{10,NCX}$	1.20		Shannon et al. (2004)
$V_{max,NCX}$	35.0	$A\ F^{-1}$	Fitted
η_{NCX}	0.70		Fitted
$k_{sat,NCX}$	4.00×10^{-2}		Shannon et al. (2004)
$n_{H,NCX}$	3.44		Fitted
H_{SERCA}	1.79		Shannon et al. (2004)
$K_{f,SERCA}$	0.28	μM	Fitted
$K_{r,SERCA}$	2.00×10^3	μM	Shannon et al. (2004)
$Q_{10,ERCa}$	2.60		Shannon et al. (2004)
$V_{max,SERCA}$	9.09	μM ms^{-1}	Schipke et al. (2008)

Table S8: Parameters for p38/NFAT Cycle/TNFα Gene Expression Calculations

Parameter	Value	Unit	Reference & Note
$k_{r,pp38}$	1.85×10^{-7}	ms^{-1}	Fitted
$k_{f,pp38}$	1.20×10^{-5}	ms^{-1}	Fitted
Kd_{pp38}	0.15×10^{-5}	arbitrary unit	Fitted
n_{pp38}	1.20×10^{-5}		Fitted
$pp38t$	100	arbitrary unit	Fitted
C_{cn}	1		Volume ratio of nucleus to cytoplasm
$NFATt$	1.2	nM	Fitted: Total amount of NFAT molecules in the microglia
$k1_{f,NFAT}$	1.69×10^{-8}	$nM^{-1} ms^{-1}$	Fitted
$k2_{f,NFAT}$	1.44×10^{-6}	ms^{-1}	Cooling et al. (2009)
$k3_{f,NFAT}$	1.62×10^{-6}	ms^{-1}	Fitted
$k4_{f,NFAT}$	4.45×10^{-7}	ms^{-1}	Fitted
$k1_{r,NFAT}$	1.93×10^{-5}	ms^{-1}	Fitted
$k3_{r,NFAT}$	4.71×10^{-8}	$nM^{-1} ms^{-1}$	Fitted
$kdeg_{RNA,TNF}$	1.35×10^{-7}	ms^{-1}	Fitted
$kdeg_{TNFa,TNF}$	1.39×10^{-5}	ms^{-1}	Fitted
$kexp_{f,TNF}$	1.11×10^{-7}	$unit^{-1} ms^{-1}$	Fitted
$kexp_{r,TNF}$	2.78×10^{-7}	ms^{-1}	Fitted
$k_{trnscrpt,TNF}$	2.78×10^{-7}	ms^{-1}	Fitted
$k_{trnsl,TNF}$	2.00×10^{-7}	ms^{-1}	Fitted
$IC50_{pp38,TNF}$	60.0	arbitrary unit	Fitted
$n_{pp38,TNF}$	5.5		Fitted

Table S9: Other Parameters in Calculations

Parameter	Value	Unit	Reference & Note
F	9.65×10^3	C mol^{-1}	Faraday Constant
r_{MG}	3.68	μm	Radius of Microglia Kongsui et al. (2014)
$r_{vol,ER/Cyt}$	8.75×10^{-2}		Volume Ratio of ER lumen to Cytosol
R	8.31	J mol^{-1} K^{-1}	Gas constant
T	310	K	
D_{ERtoCy}	1.00×10^{-6}	ms^{-1}	Fitted: Leak Rate Constant from ER to Cytoplasm
D_{ExtoCy}	2.44×10^{-3}	ms^{-1}	Fitted: Leak Rate Constant from Extracellular to Cytoplasm

Table S10: Initial States in Calculations

Variable	Value	Unit	Reference & Note
Ca_2CaM	2.92×10^{-2}	μM	Fitted
Ca_4CaM	2.92×10^{-3}	μM	Fitted
Ca_4CN	3.82×10^{-2}	μM	Fitted
$CaMCN$	5.56×10^{-2}	μM	Fitted
CaF	9.87	μM	Fitted: Calcium and Fura2 complex
CaR	74.3	μM	Fitted
$pp38$	52.6		Fitted
$NFAT_{p,c}$	8.05×10^{-1}	nM	Fitted
$NFAT_{N,n}$	2.36×10^{-1}	nM	Fitted
$NFAT_{p,n}$	1.21×10^{-1}	nM	Fitted
DNA_{TNF}	40.9	arbitrary unit	Fitted
$mRNA_{TNF}$	29.5	arbitrary unit	Fitted
$DNA-TNF$	6.93	arbitrary unit	Fitted
$TNF\alpha$	4.24×10^{-1}	arbitrary unit	Fitted
Ca_{ER}	734	μM	Fitted
Ca_i	0.10	μM	Fitted
CaB_{ext}	0.91	μM	Fitted

A.2   Figures
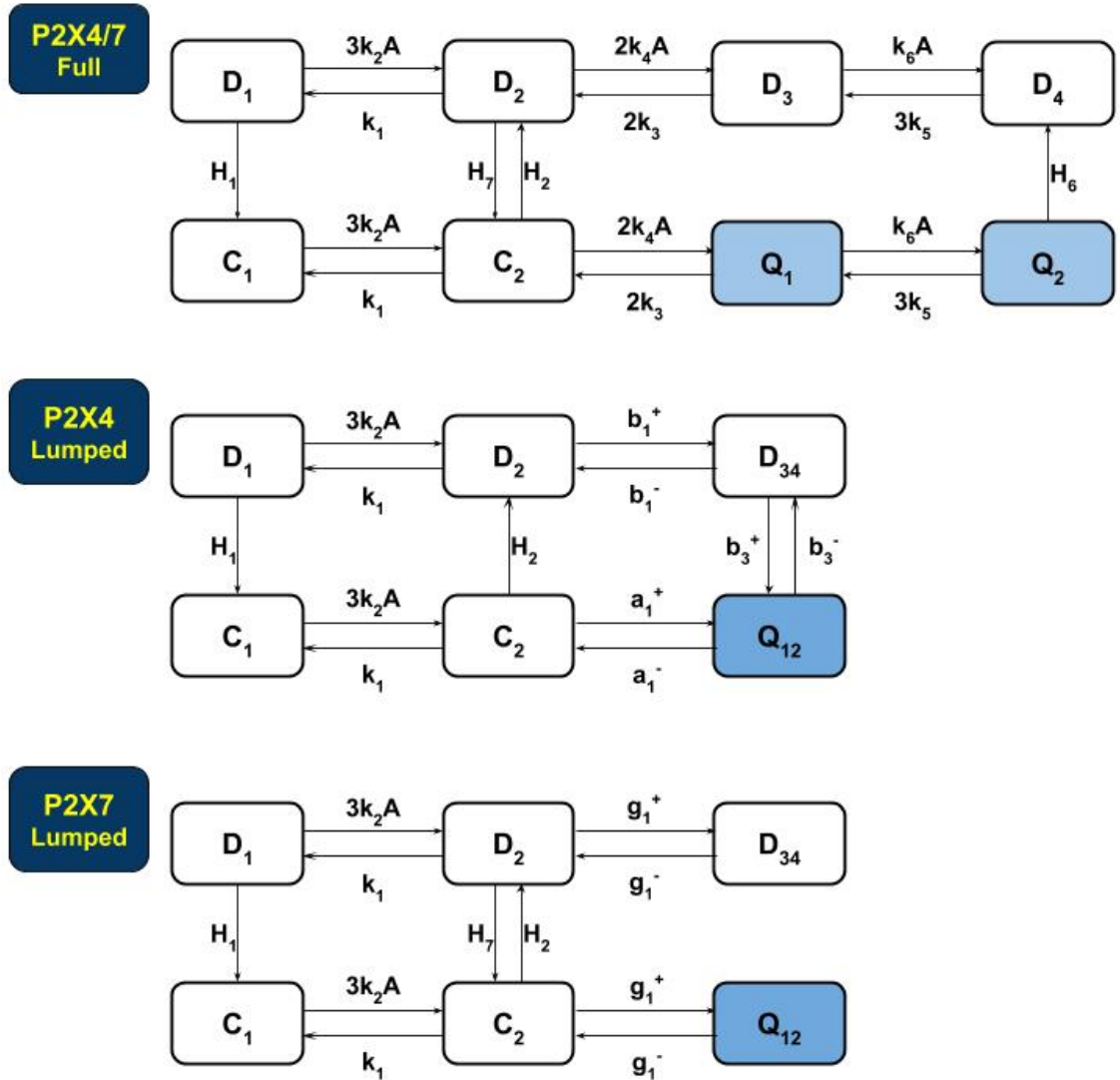
Figure S1: Markov model used for P2X channels in this study (full), for which the Q1/Q2 and D3/D4 states of the Zemkova *et al.* Zemkova et al. (2015) model (lumped) are consolidated into the 'macro states' Q12 and D34. Predictions of the Q12 'macrostate' relative to the original Q1 and Q2 states is shown in Fig. S2. .
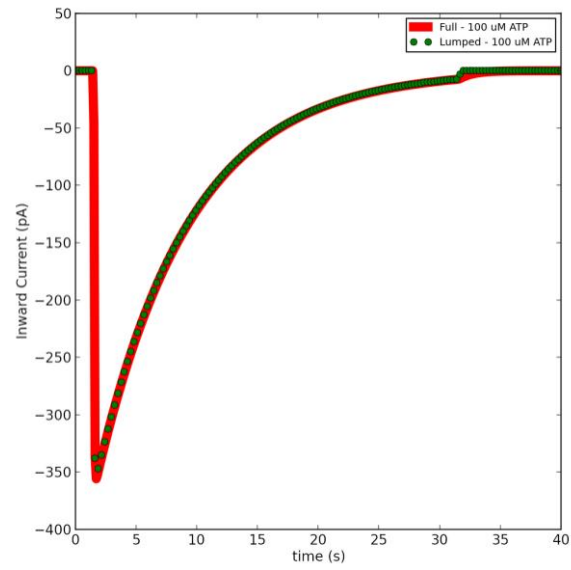
Figure S2: Comparison of model implemented from full Zemkova *et al.*Zemkova et al. (2015) model and the lumped model version used in this study. Predicted currents using the full model (red solid) and our reduced model (green bead). .
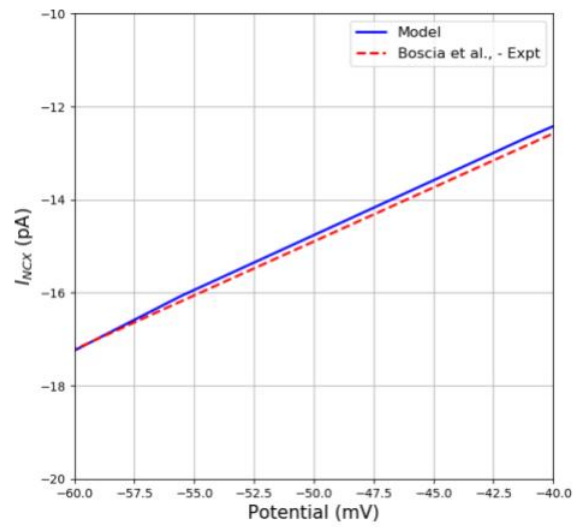
Figure S3: Outward Ca^{2+} current from NCX as a function of the cell membrane potentials. Model predictions (solid) compare well with experimental data reported in Boscia *et al.*Boscia et al. (2009) (dashed) . .
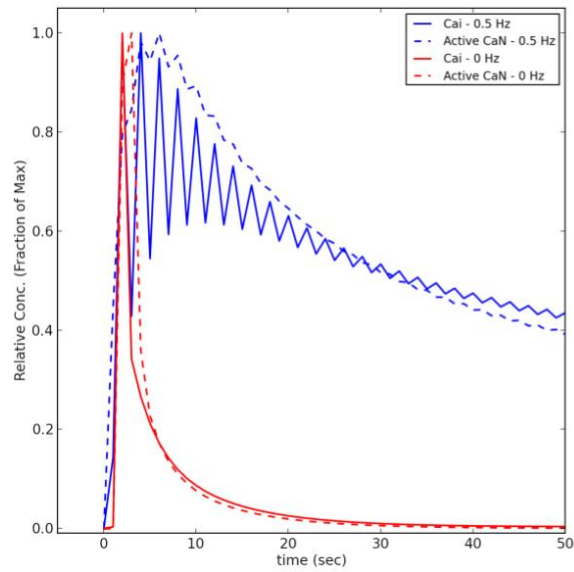
Figure S4: Predicted active calcineurin (denoted as active CN) with respect to two distinct stimulation pulses: single pulse and pulse with a frequency of 0.5 Hz. The simulated Ca^{2+} intervals in this figure were chosen to resemble those of Bazzazi *et al.* but are not quantitatively identical, given that the Bazzazi data was obtained using HEK cells. Given these Ca^{2+} transients, the timescales for rapid Ca^{2+}-dependent CN activation and delayed decline relative to the Ca^{2+} transients are shown and are analogous to comparable measurements from Bazzazi *et al.* Bazzazi et al. (2015) .
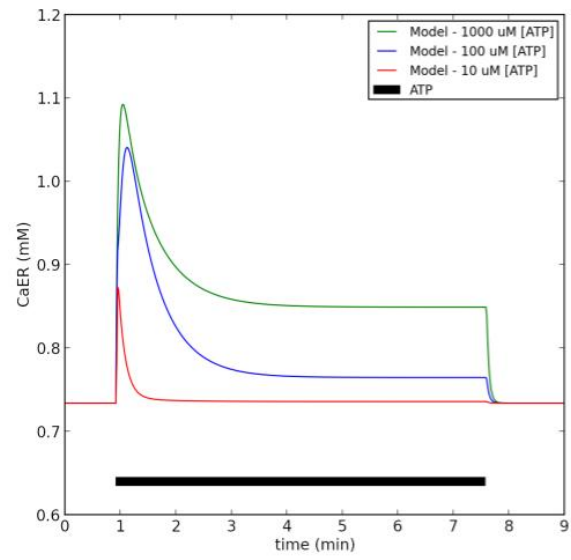
Figure S5: Predicted Ca^{2+} concentration transients in ER domain, subject to ATP treatment conditions shown in Fig. 3. .
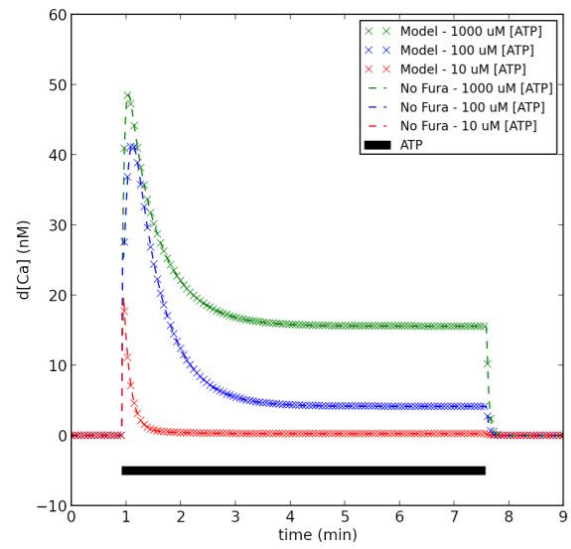
Figure S6: Predicted Ca^{2+} concentration transients with and without Fura2 in cytoplasm, subject to ATP treatment conditions shown in Fig. 3. .
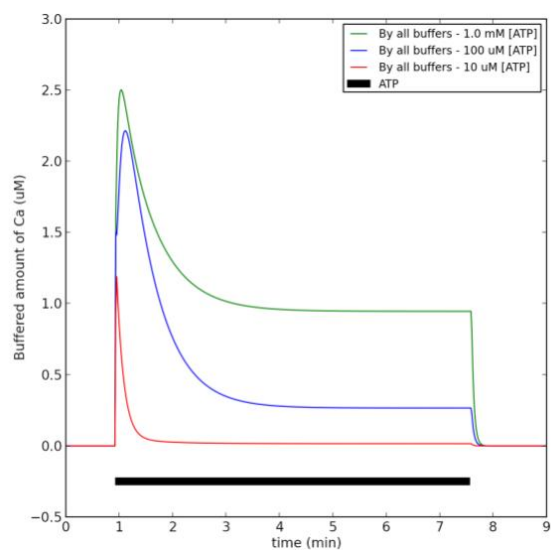
Figure S7: Predicted Ca^{2+} concentration buffered by given compounds in the model, subject to ATP treatment conditions shown in Fig. 3. .
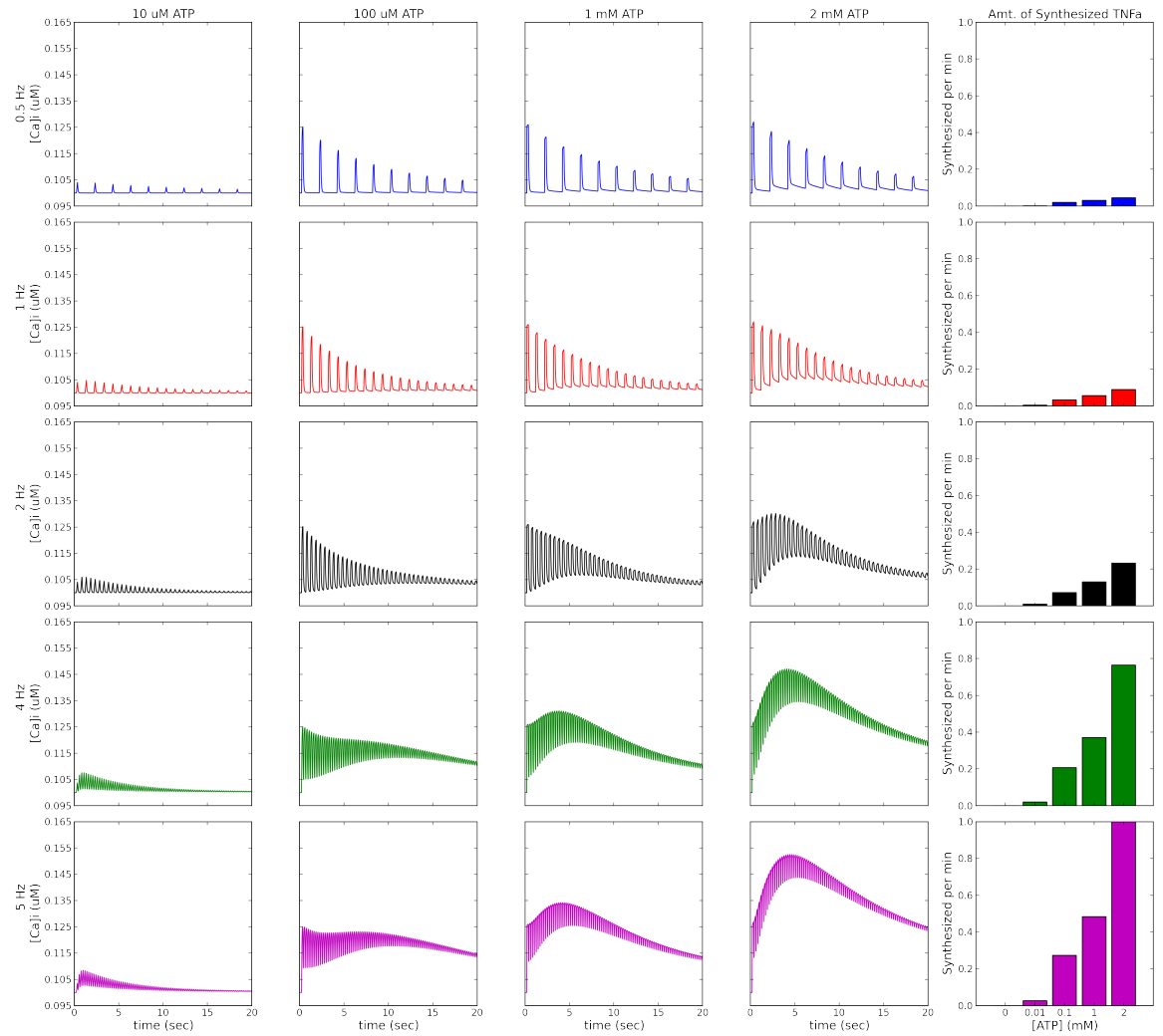
Figure S8: Cytosolic Ca^{2+} transients as a function of ATP pulse frequencies (rows) and ATP concentration (columns) as applied for 20 seconds with TNFα responses shown in the final column. .
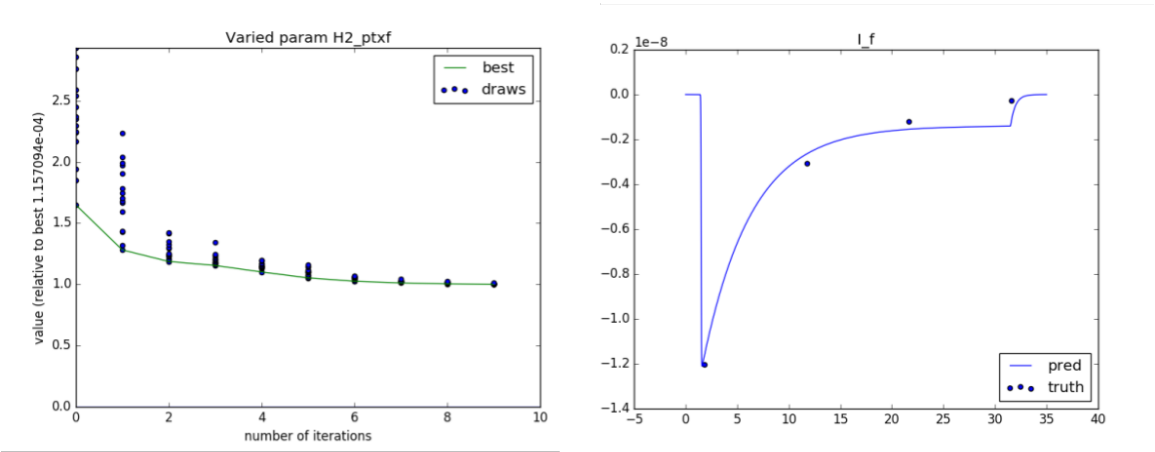
Figure S9: Left) Genetic algorithm guesses for P2X4 parameter H2. Right) Predicted current relative to Toulme *et al.*data (truth). .

A.3 Methods: Microglial Ca²⁺ model

The cytosolic Ca²⁺ pool is maintained by Ca²⁺ influxes, e.g. inward Ca²⁺ entry from PM channels and ER Ca²⁺ release, effluxes including NCX extrusion and SERCA uptake, as well as buffering by cytosolic Ca²⁺ binding proteins. A primary assumption in our model was that P2X stimulation increases cytosolic Ca²⁺ load, thereby activating downstream Ca²⁺-dependent responses. Secondly, we assumed that P2X channels, NCX, and the PM leak term were the predominant Ca²⁺ fluxes at the plasma membrane. Exchange of Ca²⁺ with an ER compartment was modeled, although the conditions assumed in this study were not expected to lead to significant ER Ca²⁺ release or decreased ER Ca²⁺ load. Ca²⁺ exchange with nuclear and mitochondrial compartments were assumed to be minor. All Ca²⁺ influx and extrusion mechanisms were directly coupled to a central cytosolic volume, within which Ca²⁺-dependent cascades were activated. Generally speaking, intracellular Ca²⁺ content was described using time-dependent differential equations that accounted for Ca²⁺ fluxes (J_i) into or out of the cytosol, as well as the summation over Ca²⁺ buffering contributions:

$$c' = J_{in} - J_{out} + \sum k_{bi} c b_i - k_{fi} c \left(b_{Ti} - c b_i \right) \tag{S1}$$

Descriptions of these components are elaborated in the following paragraphs.

A.3.1 Plasma membrane components

P2X4 The model used for P2X4 (reaction 3 in Fig. 1) is based on Zemkova *et al.* Zemkova et al. (2015) (see Fig. S1), except that we merged the Q1 and Q2 states into a single state (Q12), as well as D3 and D4 into a state D34 to simplify the model complexity, using the approach listed in Smith and Crampin (2004). We justify this consolidation of states given that the binding of two ATP molecules is sufficient to drive P2X4 opening Wang and Yu (2016) and that the consolidates D34 and Q12 states closely matched the combined probabilities of their respective underlying states (data not shown). We validated this against the experimental data in Fig. 2A. The data used for the validation was obtained by Toulme *et al.* Toulme et al. (2010), using the whole-cell patch clamp recoding technique The parameters used in this model is listed in Table S3 and were fitted to match experimental current recordings. Currents predicted for all PM Ca²⁺ fluxes were related to the rate of intracellular Ca²⁺ concentration change via

$$J = \frac{1}{nF} \frac{i_{SL}}{vol} \tag{S2}$$

where n is the valency (n=2 for Ca²⁺), F is Faraday's constant, i is a current, and *vol* is the cellular volume. Our estimate for the microglia cell volume was 0.07 pL, based on assuming a spherical cell shape with a diameter of 5.2 µmKongsui

et al. (2014). In some references, ion channel activities were expressed as current densities (amperes per Farad), in which case currents were estimated by multiplying the densities by the cell capacitance (Farad).

$$k_1^+ = 2k4_{P2X4}ATP \tag{S3}$$

$$k_1^- = 2k3_{P2X4} \tag{S4}$$

$$k_2^+ = k6_{P2X4}ATP \tag{S5}$$

$$k_2^- = 3k5_{P2X4} \tag{S6}$$

$$k_3^+ = H6_{P2X4} \tag{S7}$$

$$K_3^- = 0 \tag{S8}$$

$$K_2 = \frac{k_2^+}{k_2^-} \tag{S9}$$

$$a_1^+ = k_1^+ \tag{S10}$$

$$a_1^- = \frac{k_1^-}{1 + K_2} \tag{S11}$$

$$a_3^+ = \frac{k_3^+}{1 + \frac{1}{K_2}} \tag{S12}$$

$$a_3^- = k_3^- \tag{S13}$$

$$l_1^+ = 2k4_{P2X4}ATP \tag{S14}$$

$$l_1^- = 2k3_{P2X4} \tag{S15}$$

$$l_2^+ = k6_{P2X4}ATP \tag{S16}$$

$$l_2^- = 3k5_{P2X4} \tag{S17}$$

$$l_3^+ = a_3^- \tag{S18}$$

$$l_3^- = a_3^+ \tag{S19}$$

$$L_2 = \frac{l_2^+}{l_2^-} \tag{S20}$$

$$b_1^+ = l_1^+ \tag{S21}$$

$$b_1^- = \frac{l_1^-}{1 + L_2} \tag{S22}$$

$$b_3^+ = \frac{l_3^+}{1 + \frac{1}{L_2}} \tag{S23}$$

$$b_3^- = l_3^- \tag{S24}$$

$$D1_{P2X4} = 1 - D2_{P2X4} - D34_{P2X4} - C1_{P2X4} - C2_{P2X4} - Q12_{P2X4} \quad \text{(S25)}$$

$$\frac{dD2_{P2X4}}{dt} = 3k2_{P2X4}ATPD1_{P2X4} + H2_{P2X4} + b_1^- D34_{P2X4} \quad \text{(S26)}$$

$$- (k1_{P2X4} + b_1^+)D2_{P2X4} \quad \text{(S27)}$$

$$\frac{dC1_{P2X4}}{dt} = k1_{P2X4}C2_{P2X4} + H1_{P2X4}D1_{P2X4} \quad \text{(S28)}$$

$$- 3k2_{P2X4}ATPC1_{P2X4} \quad \text{(S29)}$$

$$\frac{dC2_{P2X4}}{dt} = 3k2_{P2X4}ATPC1_{P2X4} + a_1^- Q12_{P2X4} \quad \text{(S30)}$$

$$- (k1_{P2X4} + h2_{P2X4} + a_1^+)C2_{P2X4} \quad \text{(S31)}$$

$$\frac{dD34_{P2X4}}{dt} = b_1^+ D2_{P2X4} + b_3^- Q12_{P2X4} \quad \text{(S32)}$$

$$- (b_1^- + b_3^+)D34_{P2X4} \quad \text{(S33)}$$

$$\frac{dQ12_{P2X4}}{dt} = a_1^+ C2_{P2X4} + b_3^+ D34_{P2X4} \quad \text{(S34)}$$

$$- (b_3^- + a_1^-)Q12_{P2X4} \quad \text{(S35)}$$

P2X7   The model used for P2X7 (reaction 2 in Fig. 1) was initially based a multi-state model from Khadra *et al.* Khadra et al. (2012*a*) (see Fig. S1), although as described in the text, we merged states in rapid equilibrium to reduce the model complexity. The resulting model was validated against the experimental data from rat microglia in Fig. 2B, which demonstrates distinct responses to three ATP concentrations. This experimental data collected by Chessell *et al.* Chessell et al. (1997) was measured via the whole cell configuration of the patch-clamp technique. Moreover, as shown as 3 data sets in Fig. 2B, the 8-state model has been lumped as explained in the previous section.

For the integrated model to reproduce ATP-mediated Ca^{2+} transient of microglia, it was necessary to adjust parameters further to minimize the difference between experiment and computation. Therefore, unlike the case of P2X4 fitting, there are two sets of Markov state parameters for P2X7. The parameter set listed in Table S5 is used to reproduce the P2X7 activation mediated inward current attained by Chessell *et al.* However, this parameter set does not robustly predict the Ca^{2+} transients given in Fig. 3A, whose experimental data was ob-tained by Hide *et al.* To capture the Ca^{2+} transients data along with various ATP dosages, it was essential to prepare another set of parameters, which is listed in Table S3 and the followings.

$$k4_{P2X7} = \begin{cases} 6.00 \times 10^{-2} \, \mu\text{M}^{-1}\,\text{ms}^{-1} \text{ for } \geq 510 \, \mu\text{M ATP} \\ 0.225 \, \mu\text{M}^{-1}\,\text{ms}^{-1} \text{ otherwise} \end{cases} \quad \text{(S36)}$$

$$k6_{P2X7} = \begin{cases} 15.0 \, \mu\text{M}^{-1}\,\text{ms}^{-1} \text{ for } \geq 510 \, \mu\text{M ATP} \\ 1.0 \, \mu\text{M}^{-1}\,\text{ms}^{-1} \text{ otherwise} \end{cases} \quad \text{(S37)}$$

$$H7_{P2X7} = \begin{cases} 1.0 \times 10^{-5} \, \text{ms}^{-1} \text{ for } \geq 510 \, \mu\text{M ATP} \\ 6.2 \times 10^{-5} \, \text{ms}^{-1} \text{ otherwise} \end{cases} \quad \text{(S38)}$$

Calculation of Inward Current and Ca Influx   The calculations of Markov state models for both P2X4 and P2X7 provide the open state probability of channels that induce the inward current in microglia. Based on the Hodgkin-Huxley equation, the inward current through open channels were calculated using the conductances and membrane potentials listed in Table S3.

$$I_{P2X} = \rho_{P2X} G12_{P2X}(E12_{P2X} - V_{P2X,rev.pot.}) \tag{S39}$$

According to the outcomes of P2X4 channel characterization by Toulme *et al.*, their inward current data given in Fig. 2A is equivalent to the current measured from the activated microglia, which leads to 940 nM increase in the cytosolic Ca^{2+} concentration after stimulation by 100 uM ATP. Particularly, the current density corresponding to the profile of inward current via P2X4 in Fig. 2A (9 pA/pF) is also reported to be 30-fold higher than the measurement in rest microglia (0.3 pA/pF). This scale is used as surface density for P2X4 in our model and it is denoted as ρ_{P2X4}, so that this parameter can represent the physical difference in the degree of P2X4 expression in various states of microglial cells.

$$J_{P2X4} = \frac{-I_{P2X4}}{2F} \frac{f_{I_{Ca,P2X4}} f_{conv.,P2X4}}{Vol_{microglia}} \tag{S40}$$

It was found that the current microglia model estimated 11-fold lower Ca^{2+} influx based on the comparison between the Ca^{2+} prediction and the value reported by Toulme *et al.* To improve the prediction by our mathematical model, the scale factor, $f_{conv.,P2X4}$ was introduced in the calculation of Ca^{2+} influx calculation to recover the underestimation compared to the experimental value. For the case of P2X7, since the increase in Ca^{2+} concentration by the activation of P2X7 receptors is not reported, the set of parameters given in Table S3 was directly used without employing specific scale.

A.3.2   Na/Ca exchanger (NCX)

The NCX model was adapted from Shannon *et al.* Shannon et al. (2004) (reaction 13 in Fig. 1) and the equations used in this work are listed as Eq. S41-Eq. S52. Since the original model was based on cardiac system, parameters in Table S7 were refit. For this adjustment, the predicted NCX currents were compared against the experimental data obtained by Boscia *et al.* Boscia et al. (2009) via the patch-clamp technique in whole-cell configuration. (see Fig. S3).

$$Q_{NCX} = Q_{10,NCX}^{\frac{T-310}{10}} \tag{S41}$$

$$K_{a,NCX} = \frac{1}{1 + \left(\frac{Kd_{Act,NCX}}{Ca_i}\right)^{n_{H,NCX}}} \tag{S42}$$

$$Z = \frac{FV}{RT} \tag{S43}$$

$$\delta = Ca_e Na_i^{H_{Na,NCX}} \tag{S44}$$

$$\sigma = Na_e^{H_{Na,NCX}} Ca_i \tag{S45}$$

$$top_{NCX} = V_{max,NCX} \left(-e^{(-1+\eta_{NCX})Z}\sigma + \delta e^{\eta_{NCX}Z} \right) K_{a,NCX} Q_{NCX} \tag{S46}$$

$$bot_{NCX} = \left(1 + k_{sat,NCX} Z e^{-1+\eta_{NCX}} \right) \tag{S47}$$

$$\times (K_{max,Ca_i,NCX} Na_{e,NCX}^{H_{Na,NCX}} \left(1 + \left(\frac{Na_i}{K_{max,Na_i,NCX}} \right)^{H_{Na,NCX}} \right) \tag{S48}$$

$$+ K_{max,Na_e,NCX}^{H_{Na,NCX}} \left(1 + \frac{Ca_i}{K_{max,Ca_i,NCX}} \right) Ca_i \tag{S49}$$

$$+ K_{max,Ca_e,NCX} Na_{i,NCX}^{H_{Na,NCX}} + \delta + \sigma) \tag{S50}$$

$$I_{NCX} = \frac{top_{NCX}}{bot_{NCX}} \tag{S51}$$

$$J_{NCX} = \frac{C_{mem} I_{NCX}}{Vol_{MG} F} \tag{S52}$$

A.3.3 Membrane Ca^{2+} leaks

To ensure that cytosolic and ER Ca^{2+} content were constant at rest, inward Ca^{2+} and outward ER Ca^{2+} leaks were introduced, as done similarly in other models of eukaryotic Ca^{2+} handling. These adaptations were necessary, as NCX Ca^{2+} efflux and SERCA Ca^{2+} uptake are significant, even at resting conditions. Correspondingly, reactions 7 and 8 were based on formula described in Eq. S53 and Eq. S54.

$$J_{ExtoCy} = D_{ExtoCy} \left(Ca_e - Ca_i \right) \tag{S53}$$

$$J_{ERtoCy} = D_{ERtoCy} \left(Ca_{ER} - Ca_i \right) \tag{S54}$$

A.3.4 Cytosolic Ca^{2+} handling

Cytosolic Ca^{2+} content in our model is controlled by the Ca^{2+} fluxes arising from the P2X channels, plasma membrane and ER Ca^{2+} leaks, buffering with CaM, CN and indicator, as well as contributions from NCX and SERCA. These

are summarized below

$$\frac{dCa_i}{dt} = J_{P2X7} + J_{P2X4} + J_{ExtoCy} + J_{ERtoCy} + J_{SERCA} + J_{NCX} \tag{S55}$$

$$- \frac{dCa_2CaM}{dt} - \frac{dCa_4CN}{dt} - \frac{dCa_4CaM}{dt} - \frac{dCaF}{dt} - \frac{dCaB_{ext}}{dt} \tag{S56}$$
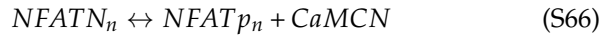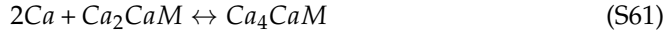
Ca^{2+}buffering   In eukaryotes, Ca^{2+} is strongly buffered Berridge et al. (2003) (reaction 1 in Fig. 1). To a limited extent, the reactions contributing to CaM and CN activation buffer cytosolic Ca^{2+}. However, we introduced an additional buffering term described in Eq. S57 to account for the relatively small increases in cytosolic Ca^{2+} upon activation of P2X channels. Parameters for this contribution are listed in Table S6.

$$\frac{dCaF}{dt} = k_{on,Fura} \left(B_{max,Fura} - CaF \right) Ca_i - k_{off,Fura} CaF \tag{S57}$$

$$\frac{dCaB_{ext}}{dt} = k_{on,B,extra} \left(B_{max,B,extra} - CaB_{ext} \right) Ca_i - k_{off,B,extra} CaB_{extra} \tag{S58}$$

$$\frac{dCaR}{dt} = k_{on,Calr,ER} \left(B_{max,Calr,ER} - CaR \right) Ca_{ER} - k_{off,Calr,ER} CaS \tag{S59}$$

Ca^{2+}→CaM→CaN→NFAT   In our model, free Ca^{2+} catalyzes CN activation via binding CaM. (reaction 1 in Fig. 1). The mathematical model proposed by Bazzazi *et al.* Bazzazi et al. (2015) was implemented and the equations and parameters used in the model are listed in Eq. S68-Eq. S76 and Table S6. Following the model proposed by Cooling *et al.* Cooling et al. (2009), the activated CN complex determines the rate of dephosphorylating the NFAT transcription factor (reaction 10 and 12). These relationships are given by Eq. S77-Eq. S85 along with parameters listed in Table S8. The predicted content of NFAT transcription factor was validated via its comparison to the experimental data obtained by Ferrari *et al.*Ferrari et al. (1999*b*) in Fig. 4.

$$2Ca + CaM \leftrightarrow Ca_2CaM \tag{S60}$$
$$2Ca + Ca_2CaM \leftrightarrow Ca_4CaM \tag{S61}$$
$$2Ca + Ca_2CN \leftrightarrow Ca_4CN \tag{S62}$$
$$Ca_4CaM + Ca_4CN \leftrightarrow CaMCN \tag{S63}$$
$$NFATp_c + CaMCN \leftrightarrow NFATN_c \tag{S64}$$
$$NFATN_c \rightarrow NFATN_n \tag{S65}$$
$$NFATN_n \leftrightarrow NFATp_n + CaMCN \tag{S66}$$
$$NFATNp_n \rightarrow NFATp_c \tag{S67}$$

$$CaM = CaMt - Ca_2CaM - CaMCN - Ca_4CaM \tag{S68}$$

$$Ca_2CN = CNt - Ca_4CN - CaMCN \tag{S69}$$

$$\frac{dCa_2CaM}{dt} = k_{ab,CaMCN}(Ca_i)^2CaM - k_{bc,CaMCN}(Ca_i)^2Ca_2CaM \tag{S70}$$

$$+ k_{cb,CaMCN}Ca_4CaM - k_{ba,CaMCN}Ca_2CaM \tag{S71}$$

$$\frac{dCa_4CaM}{dt} = -k_{cb,CaMCN}Ca_4CaM - k_{on,A,CaMCN}Ca_4CNCa_4CaM \tag{S72}$$

$$+ k_{bc,CaMCN}(Ca_i)^2Ca_2CaM + k_{off,A,CaMCN}CaMCN \tag{S73}$$

$$\frac{dCa_4CN}{dt} = k_{on,B,CaMCN}(Ca_i)^2Ca_2CN - k_{on,A,CaMCN}Ca_4CNCa_4CaM \tag{S74}$$

$$- k_{off,B,CaMCN}Ca_4CN + k_{off,A,CaMCN}CaMCN \tag{S75}$$

$$\frac{dCaMCN}{dt} = -k_{off,A,CaMCN}CaMCN + k_{on,A,CaMCN}Ca_4CNCa_4CaM \tag{S76}$$

$$actN_{NFAT} = \frac{CaMCN}{CNt} \tag{S77}$$

$$NFAT_{N,c} = -NFAT_{p,c} + NFATt - NFAT_{N,n} - NFAT_{p,n} \tag{S78}$$

$$R_{1,NFAT} = -k1_{r,NFAT}\left(1 - actN_{NFAT}\right)NFAT_{N,c} + k1_{f,NFAT}NFAT_{p,c}CaMCN \tag{S79}$$

$$R_{2,NFAT} = k2_{f,NFAT}NFAT_{N,c} \tag{S80}$$

$$R_{3,NFAT} = k3_{f,NFAT}\left(1 - actN_{NFAT}\right)NFAT_{N,n} - k3_{r,NFAT}NFAT_{p,n}CaMCN \tag{S81}$$

$$R_{4,NFAT} = k4_{f,NFAT}NFAT_{p,n} \tag{S82}$$

$$\frac{dNFAT_{p,c}}{dt} = \frac{R_{4,NFAT}}{C_{cn}} - R_{1,NFAT} \tag{S83}$$

$$\frac{dNFAT_{N,n}}{dt} = -R_{3,NFAT} + C_{cn}R_{2,NFAT} \tag{S84}$$

$$\frac{dNFAT_{p,n}}{dt} = -R_{4,NFAT} + R_{3,NFAT} \tag{S85}$$

Ca→p38 pp38 indirectly regulates cytokine synthesis at a post-transcriptional level by inactivating an enzyme that destabilizes mRNA stability in the cytosol and inhibits translation. Menon and Gaestel (2018). Thus we use a phenomenological model to link p38 activation (e.g. formation of its phosphorylated state) to delayed degradation of TNFα mRNA (reaction 9 in Fig. 1). Further, in accordance with Wright *et al.* Wright et al. (2007), we assumed p38 phosphorylation is Ca^{2+} dependent. Accordingly, we introduced the expressions Eq. S86 and Eq. S87, for which parameters are listed in Table S7.

$$p38 = pp38t - pp38 \tag{S86}$$

$$\frac{dpp38}{dt} = -k_{b,pp38}pp38 + k_{f,pp38}Ca_ip38 \tag{S87}$$

A.3.5 Transcriptional regulation

In accordance with Hide *et al.*, we assumed TNFα release was dependent on NFAT and p38 activation Hide et al. (2000). For NFAT regulation, we assume that nucleus-localized dephosphorylated (active) NFAT binds directly to promoter regions on associated genes (reviewed in Hogan et al. (2003)) (reaction 12 in Fig. 1), after which TNFα mRNA is transcribed. As a refinement to the Hide *et al.* data, we additionally assumed TNFα exocytosis proceeds in a Ca^{2+}- and P2X7-dependent manner, in congruence with data collected in macrophages Stanley and Lacy (2010) and microglia Kataoka et al. (2009). expressions following Eq. S88 quantify these processes and are informed with parameters listed in Table S8.

$$R_{transcript,TNF} = k_{trnscrpt,TNF}DNA_{TNF}NFAT_{N,n} \tag{S88}$$

$$R_{translate,TNF} = k_{trnsl,TNF}mRNA_{TNF} \tag{S89}$$

$$R_{deg,TNF\alpha_{TNF}} = kdeg_{TNF\alpha_{TNF}}TNF\alpha \tag{S90}$$

$$R_{deg,RNA_{TNF}} = \left(\frac{kdeg_{RNA_{TNF}}}{1 + \left(\frac{pp38}{IC50_{pp38,TNF}} \right)^{n_{pp38,TNF}}} \right) mRNA_{TNF} \tag{S91}$$

$$R_{exp,TNF} = kexp_{f,TNF}DNA_{TNF}TNF\alpha - kexp_{r,TNF}DNATNF \tag{S92}$$

$$\frac{dDNA_{TNF}}{dt} = -R_{exp,TNF} \tag{S93}$$

$$\frac{dmRNA_{TNF}}{dt} = R_{transcript,TNF} - R_{deg,RNA_{TNF}} \tag{S94}$$

$$\frac{dDNATNF}{dt} = R_{exp,TNF} \tag{S95}$$

$$\frac{dTNFa}{dt} = R_{translate,TNF} - R_{deg,TNF\alpha_{TNF}} - R_{exp,TNF} \tag{S96}$$

A.3.6 Endoplasmic reticulum

Sarcoplasmic/endoplasmic reticulum calcium ATPase (SERCA)   In addition to the ER leak described earlier, we assume ER Ca^{2+} content is determined by SERCA activity. The functional form for the SERCA model is adapted from Shannon *et al.*Shannon et al. (2004). The rate is dependent on the intracellular and ER Ca^{2+} content, as well as a maximum turnover rate, $Vmax$, which is a reflection of the total intracellular content of functional SERCA. Given the lack of data to parameterize SERCA uptake in glia, we utilized parameters from

Shannon *et al.* for this component.

$$Q_{ERCa} = Q_{10,ERCa}^{\frac{T-310}{10}} \tag{S97}$$

$$top_{SERCA} = \left(\frac{Ca_i}{K_{f,SERCA}}\right)^{H_{SERCA}} - \left(\frac{Ca_{ER}}{K_{r,SERCA}}\right)^{H_{SERCA}} \tag{S98}$$

$$bottom_{SERCA} = 1 + \left(\frac{Ca_i}{K_{f,SERCA}}\right)^{H_{SERCA}} + \left(\frac{Ca_{ER}}{K_{r,SERCA}}\right)^{H_{SERCA}} \tag{S99}$$

$$J_{ERtoCyt} = Q_{ERCa} V_{max,SERCA} \frac{top_{SERCA}}{bottom_{SERCA}} \tag{S100}$$

$$J_{CyttoER} = r_{vol,ER/Cyt} J_{ERtoCyt} \tag{S101}$$

A.4   Methods:Fitting via genetic algorithm

Using our genetic algorithm (GA) initially developed in Stewart *et al.* Stewart et al. (2018), we optimized several model parameters to reproduce time-dependent experimental data. For this study, we extended the genetic algorithm (GA) primarily to include simultaneous variations of multiple parameters as well as multi-resolution time stepping. The key steps are as follows:

- Given an initial parameter value, a lognormally distributed ensemble of random variates, n_i, are drawn (10 or more), which rescale the parameter value by $1/n_i$ and n_i. The lognormal distribution was chosen to ensure that reductions and increases of N% were equally probable.
- The microglial model is simulated for appropriate time-lengths, using each member of the randomized parameter ensemble. The observable, which may consist of scalars (e.g. for concentration) or time-dependent profiles (e.g) for channel currents are collected for comparison in the next step.
- The relative error between the model using variate n_i and the corresponding experimental data is assessed via a 'fitness score' defined as

$$jobFitness_i = \sum_j (X_{i,j,pred} - X_{j,expt})^2 \tag{S102}$$

where $j = 1$ for a scalar value and $j > 1$ otherwise.
- The random variate with the smaller fitness score is stored as the new initial parameter value for subsequent optimization iterations.
- The standard deviation of the lognormal distribution, σ, is reduced each iteration, j, as

$$\sigma_{j+1} = \sigma_0 e^{-jr} \tag{S103}$$

where r controls the convergence rate.

These steps are repeated until the convergence expression

$$\lambda = \frac{\sqrt{jobFitness}}{X_{expt}} \tag{S104}$$

yield tolerances below 1% ($\lambda < 1\%$). This algorithm's performance in refitting the current profiles for P2X4is shown in Fig. S9.